# A novel adjustable PHBV basement film for enhancing the efficacy of glaucoma surgery by inhibiting scar formation

Dengming Zhou [a],[1], Wenxiang Zhu [b],[1], Hairong Liu [b],[**], Feng Zhang [c], Xiaoyu Zhou [a], Xinyue Zhang [a], Yang Zhao [a], Yuting Huang [d], Xuanchu Duan [a],[*]

[a] Aier Glaucoma Institute, Hunan Engineering Research Center for Glaucoma with Artificial Intelligence in Diagnosis and Application of New Materials, Changsha Aier Eye Hospital, Changsha, China, 410015
[b] College of Materials Science and Engineering, Hunan University, Changsha, 410082, China
[c] The Third Xiangya Hospital, Central South University, Changsha, 410013, China
[d] Shanghai Achieva Medical Suzhou Co., Ltd. Suzhou, 215028, China

## ARTICLE INFO

## ABSTRACT

Trabeculectomy is the primary surgical approach used to treat glaucoma, but scarring of the filtering passage (filtering bleb) after surgery often leads to treatment failure. To address this issue, we have developed a drug release system called RSG/Pd@ZIF-8 PHBV film. This system enables the sustained release of an anti-fibrosis drug, aiming to prevent scarring. *In vitro*, the film has the function of continuous Rosiglitazone (RSG) release, with accelerated release after laser irradiation. The antibacterial experiments revealed that the film exhibited antibacterial rates of 87.0 % against E.coli and 97.1 % against S.aureus, respectively. Moreover, we confirmed its efficacy in a rabbit eye model undergoing trabeculectomy. After implantation of the film, we observed a prolonged postoperative period for reducing intraocular pressure (IOP), increased survival rate of filtering blebs, and improved long-term surgical outcomes *in vivo*. Additionally, the film exhibited excellent biosafety. In summary, the designed sustained-release film in this study possesses the aforementioned functionalities, allowing for the regulation of anti-scarring drug release without causing harm post-surgery. This personalized and precise anti-scarring strategy represents a significant advancement.

## 1. Introduction

Glaucoma is the leading cause of irreversible blindness worldwide [1–3]. According to a global epidemiological survey conducted in 2013, the prevalence of glaucoma among individuals over the age of 40 was 3.54 %, accounting for approximately 64 million patients. It is predicted that the number of glaucoma patients worldwide will increase to 112 million by 2040 [1]. In order to control the progression of glaucoma and preserve visual field, the only proven effective measure is to control intraocular pressure (IOP) [4–6]. Clinicians achieve IOP control through the use of medications, laser treatments, and surgery [7,8]. However, fibrosis of the filtering pathway following glaucoma filtering surgery (GFS) remains a major obstacle to achieving long-term reduction in IOP [9–11]. Therefore, there is a need for improvement in the use of anti-metabolic drugs such as Mitomycin C (MMC) and 5-fluorouracil (5-Fu)

during surgery to prevent fibrosis of the filtering pathway.

Due to the average efficacy of MMC and 5-Fu and their associated side effects, ophthalmic scientists are dedicated to developing novel anti-scarring drugs or drug delivery systems. Rosiglitazone (RSG) is a PPARγ agonist with PPARγ receptors distributed in various tissues [12]. Researchers have discovered multiple extraglycemic applications of rosiglitazone, including its anti-inflammatory properties, ability to combat hepatic fibrosis, and potential in treating chronic kidney disease and Alzheimer's disease [13–17]. In recent years, numerous studies have confirmed the anti-fibrotic properties of rosiglitazone in different organs and tissues [14,17]. Previous research conducted by our group has revealed that rosiglitazone effectively inhibits the TGF β-induced phenotypic transformation of human Tenon's fibroblasts (HTFs) and may reduce fibrosis in HTFs through the Beclin1-VPS34-ATG14L autophagy pathway [18,19]. Due to genetic and environmental factors, the

---

time and extent of postoperative scar formation in the filtering pathway can vary among patients. To address these clinical challenges, the development of a nanotechnology-based drug delivery system capable of locally and effectively releasing less toxic anti-fibrotic drugs, while allowing non-invasive and personalized regulation of drug release rates, holds significant clinical importance.

We have developed a composite nano drug delivery system called rosiglitazone/palladium@zeolite imidazole ester skeleton-8 poly-hydroxybutyrate valerate (RSG/Pd@ZIF-8 PHBV) sustained-release film, which incorporates near-infrared (NIR) responsive drug release rosiglitazone. The film consists of Pd nanosheets, a novel two-dimensional nanomaterial with excellent photothermal conversion properties, and ZIF-8, a zinc-rich nanoparticle with antibacterial effects in a regular octahedral configuration. Zinc is an essential trace element that plays a crucial role in various physiological functions in the body, including the regulation of tissue and organ fibrosis, as supported by clinical and laboratory studies [20–23]. To achieve NIR-responsive drug release, we will employ a one-pot method to prepare RSG/Pd@ZIF-8 nanoparticles (RSG/Pd@ZIF-8 NPs), which facilitates the accelerated release of rosiglitazone upon near-infrared laser irradiation [24,25]. Considering that nanoparticles can be easily engulfed by cells and are not easily present in the local area for an extended period due to the long-term washing away of the filtration passage by aqueous humor, we have designed the film to anchor the nanoparticles within an electro-spinning matrix. Polyhydroxybutyrate valerate (PHBV), a member of the Polyhydroxyalkanoates (PHA) family known for its biodegradability, serves as the substrate for the film. Kim et al. found that PHBV electrospinning films can reduce scar formation during skin wound healing [26]. Our team accumulated experience in PHBV electrospinning technology and incorporated RSG into PHBV films [19,27]. Overall, The biodegradability of PHBV is very suitable for the anti scar field of glaucoma surgery. By incorporating RSG/Pd@ZIF-8 into the electrospinning solution, we can fabricate the RSG/Pd@ZIF-8 PHBV film (see Fig. 1).

## 2. Results and discussion

### 2.1. Synthesis and characterization of RSG/Pd@ZIF-8 NPs

Palladium nanosheets (Pd) were first prepared under the protection of carbon monoxide. RSG/Pd@ZIF-8 NPs were synthesized using a one-pot method, where Pd and RSG were added during the ZIF-8 self-assembly process. General photographs of solutions containing ZIF-8, Pd@ZIF-8, and RSG/Pd@ZIF-8 NPs are shown below (Fig. S1). The morphology of ZIF-8, Pd@ZIF-8 and RSG/Pd@ZIF-8 NPs was observed using scanning electron microscopy (SEM) and transmission electron microscopy (TEM) (Fig. 2A–C). The Pd exhibited a two-dimensional hexagonal configuration, with sizes ranging mostly from 13 to 17 nm (Fig. S2). ZIF-8 and Pd@ZIF-8 NPs displayed distinct octahedral configurations under electron microscopy. After loading rosiglitazone (RSG/Pd@ZIF-8), RSG/Pd@ZIF-8 lost its regular form, and the surface became rough, with a slight increase in size compared to Pd@ZIF-8 but comparable to ZIF-8. Furthermore, the precise sizes of ZIF-8, Pd@ZIF-8, and RSG/Pd@ZIF-8 NPs were measured using dynamic light scattering (DLS) (Fig. 2D–F). There was a small difference in size between ZIF-8 (~220 nm) and RSG/Pd@ZIF-8 (~220 nm), while Pd@ZIF-8 had the
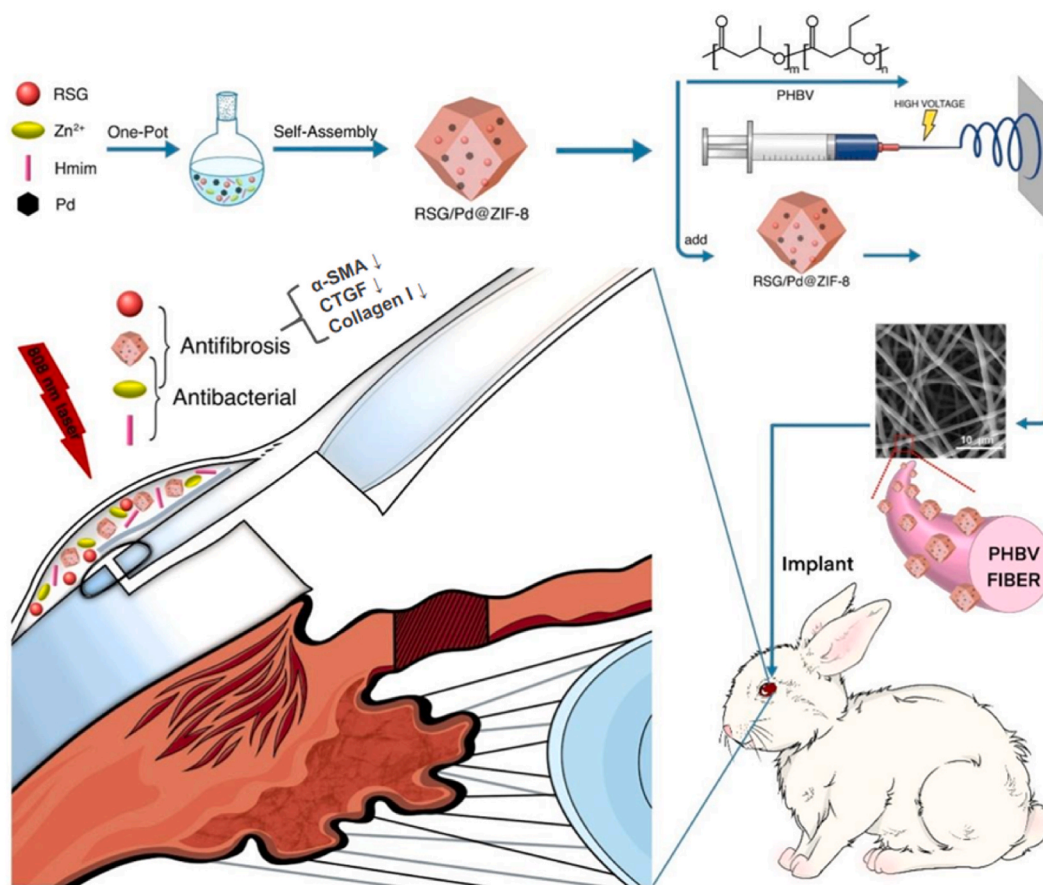


**Fig. 1.** A schematic diagram of the technical roadmap for constructing a new nano drug delivery platform. It can be divided into three parts. Part I, Synthesis of drug loaded nanoparticles. Part II, Preparation of PHBV sustained-release membranes containing nanoparticles. Part III, the study of anti scar formation effect and safety of sustained-release membranes implanted in rabbit filtration surgery. RSG, Rosiglitazone. Hmim,2-methylimidazole. Pd, palladium nanosheets. PHBV, poly hydroxybutyrate-co-valerate.
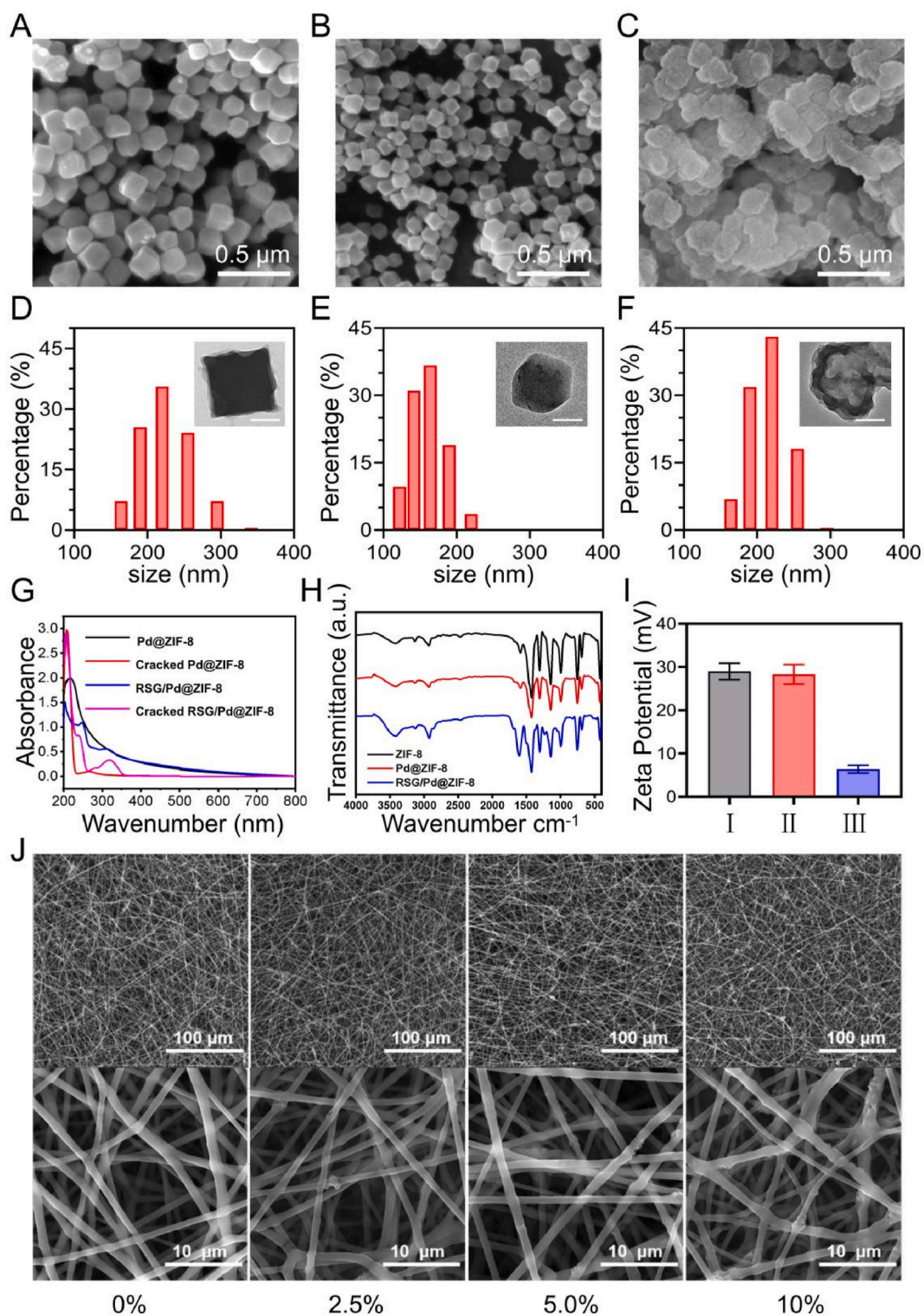
**Fig. 2.** SEM image of ZIF-8 (A), Pd@ZIF-8 (B) and RSG/Pd@ZIF-8 (C). SEM image and hydrodynamic size of ZIF-8(D), Pd@ZIF-8 (E) and RSG/Pd@ZIF-8 (F); Scale bar size is 100 nm. UV spectrum (G) and FTIR spectra (H). The I, II and III of zeta potentials (I) mean ZIF-8, Pd@ZIF-8 and RSG/Pd@ZIF-8. SEM image of RSG/Pd@ZIF-8 PHBV film with different concentrations of NPs/PHBV ratio (J).

smallest size (~160 nm).

UV–Vis spectra revealed that RSG/Pd@ZIF-8 exhibited an absorption peak at 315 nm, whereas Pd@ZIF-8 did not show such a peak. The difference in absorption peaks between the two nanoparticle types became more evident after hydrochloric acid cracking (Fig. 2G). Fourier transform infrared (FTIR) analysis demonstrated that RSG/Pd@ZIF-8

NPs exhibited new peaks at 1240 cm^-1, 1606 cm^-1, and 1690 cm^-1, corresponding to aryl-ether bands, vibrational peaks of carbon-oxygen double bonds, and benzene rings, respectively (Fig. 2H). X-ray diffraction (XRD) results indicated that the crystal structure of Pd@ZIF-8 NPs remained unchanged after the introduction of RSG (Fig. S3). The zeta potentials of ZIF-8, Pd@ZIF-8, and RSG/Pd@ZIF-8 NPs were measured

as 28.9 mV, 28.3 mV, and 6.4 mV, respectively (Fig. 2I). The loading capacity and encapsulation efficiency of RSG were determined as 27.8 % and 50.5 %, respectively, based on the standard curve (Fig. S4).

## 2.2. Synthesis and characterization of RSG/Pd@ZIF-8 PHBV film

The surface morphology of PHBV films doped with various concentrations of RSG/Pd@ZIF-8 NPs was observed using SEM (Fig. 2J). The film surface displayed embedded fibers with visible particles, and as the concentration of doped RSG/Pd@ZIF-8 nanoparticles increased, the number of surface particles also increased. However, there was no significant change in fiber diameter among the components within a certain concentration range, with fiber diameters ranging from approximately 1-10 μm. When the mass ratio of doped RSG/Pd@ZIF-8 NPs to PHBV reached 10 %, the surface fibers of the film appeared thicker, and agglomeration between the fibers was observed. The SEM analysis also allowed for the observation of PHBV films doped with different concentrations of Pd@ZIF-8 NPs, exhibiting similar morphology (Fig. S5).

## 2.3. Cytotoxicity study

To evaluate the cytotoxicity of Pd@ZIF-8, RSG/Pd@ZIF-8 NPs, and RSG/Pd@ZIF-8 PHBV film, we conducted Cell Counting Kit-8 (CCK-8) assays. HFTFs cells were co-cultured with different concentrations of these materials for 24 h. The results showed that toxicity of Pd@ZIF-8 started to manifest at 50 μg/mL, while toxicity of RSG/Pd@ZIF-8 appeared at 60 μg/mL (Fig. 3A and B). Based on the CCK-8 test, we selected a 2.5 % concentration sustained-release film as the main experimental material due to its lower toxicity (Fig. 3C).

In the hemolysis test using rabbit blood cells, the RSG/Pd@ZIF-8 PHBV film with mass fractions of 2.5 %, 5.0 %, and 10 % demonstrated hemolysis rates of 0.25 %, 1.69 %, and 3.45 %, respectively (Fig. 3D). The overall observation of the rabbit blood cell hemolysis test was displayed in an Eppendorf tube (Fig. S6).

SEM observation revealed that fibroblast growth was observed on the surface of the RSG/Pd@ZIF-8 PHBV film. The fibroblasts exhibited a normal size, elongated spindle shape, and maintained a normal cell density and quantity. No significant cell shrinkage or fragmentation was observed (Fig. 3E).
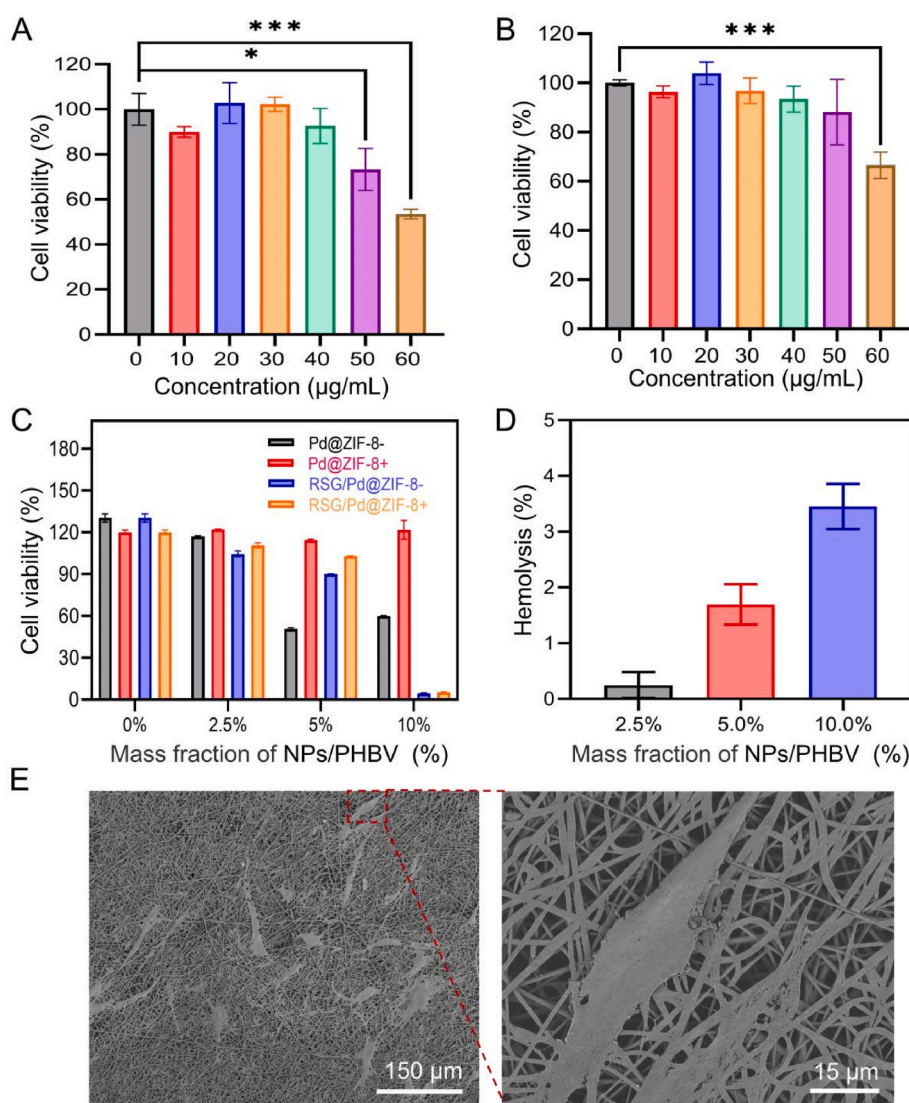


**Fig. 3.** The toxicity of Pd@ZIF-8 (A) and RSG/Pd@ZIF-8 (B) using CCK-8 trials. The toxicity of Pd@ZIF-8 PHBV and RSG/Pd@ZIF-8 PHBV films of different concentrations using CCK-8 trials (C). Rabbit red blood cell hemolysis experiment of different concentrations of RSG/Pd@ZIF-8 PHBV films (D). SEM observation of HTFs adhering to the RSG/Pd@ZIF-8 PHBV films (E).

## 2.4. Photothermal effect

Under laser irradiation with a wavelength of 808 nm, the films in the 0.0 %, 2.5 %, 5.0 %, and 10 % groups exhibited heating effects, and the heating rate and peak temperature increased with increasing nanoparticle concentration. At a background temperature of 32 °C, the peak temperatures reached 32.5 °C, 45 °C, 47.5 °C, and 50 °C, respectively, after 3 min (Fig. 4A and B). For the 2.5 % RSG/Pd@ZIF-8 PHBV film under 808 nm laser irradiation, the heating rate and peak temperature increased with the laser power. At a background temperature of 32 °C, peak temperatures of 37.5 °C, 45 °C, 55 °C, and 72.5 °C could be achieved with laser powers of 150 mW, 250 mW, 350 mW, and 450 mW, respectively (Figs. S7 and 4C). The RSG/Pd@ZIF-8 PHBV film has excellent photothermal cycling curve (Fig. 4D). Moreover, the RSG/Pd@ZIF-8 PHBV sustained-release film prepared in this study exhibited photoacoustic imaging capability. The photoacoustic signal was enhanced with an increase in the mass of nanoparticles in the film, and within a certain range of laser power, there was a linear correlation between the mass of nanoparticles in the film and the photoacoustic signal (Fig. S8).

## 2.5. Drug release test

Under pH 5.1 or 808 nm laser irradiation, the concentration of Rosiglitazone in the liquid released from the film increased over time (16.0 % release in the control group on the 28th day; 24.5 % in the laser irradiation group; 27.5 % in the pH 5.1 group). These results confirmed the dual response characteristics of the film, where it responded to near-infrared light (NIR), at a wavelength of 808 nm, and pH to release Rosiglitazone (Fig. 4E).

## 2.6. In vitro anti-fibrosis of RSG/Pd@ZIF-8 PHBV film

The RT-PCR results demonstrated that the RSG/Pd@ZIF-8 PHBV film significantly inhibited the differentiation of fibroblasts (HTFs) into myofibroblasts induced by TGF-$\beta$1. Additionally, the film's anti-fibrotic ability was further enhanced by irradiation with a laser wavelength of 808 nm (Fig. 4F).

## 2.7. Antibacterial activities of RSG/Pd@ZIF-8 PHBV film

The bacterial plate counting experiment revealed that the RSG/Pd@ZIF-8 PHBV film exhibited bactericidal properties, killing 63.5 % of *Escherichia coli* and 84.5 % of *Staphylococcus aureus* without laser irradiation. Under laser irradiation, the sterilization effect of the film increased to 87.0 % and 97.1 % (Fig. 5A–D). The anti-bacterial ability of the RSG/Pd@ZIF-8 PHBV membrane was assessed using the Live & Dead Bacterial Staining Kit. Confocal microscopy images showed that both *E. coli* and *S. aureus* stained with orange fluorescence (a combination of red and green fluorescence), lost their regular form, and agglomerated into clusters (Fig. 5E). Furthermore, SEM observations revealed that bacterial cell membranes shrank, lost their regular morphology, agglomerated into clusters, and their numbers greatly decreased (Fig. 5F).

## 2.8. Observation on the effect of RSG/Pd@ZIF-8 PHBV film implantation in rabbits trabeculectomy

Digital photography was used to record the local morphology of rabbit eyes on the 7th, 14th, and 28th days after trabeculectomy (Fig. 6A), with the location of the filter blebs indicated by white arrows. In the sham group and group C, flattened filtering blebs were observed on all three observation days. As the observation period increased, the range of filtering blebs gradually decreased, and more blood vessels
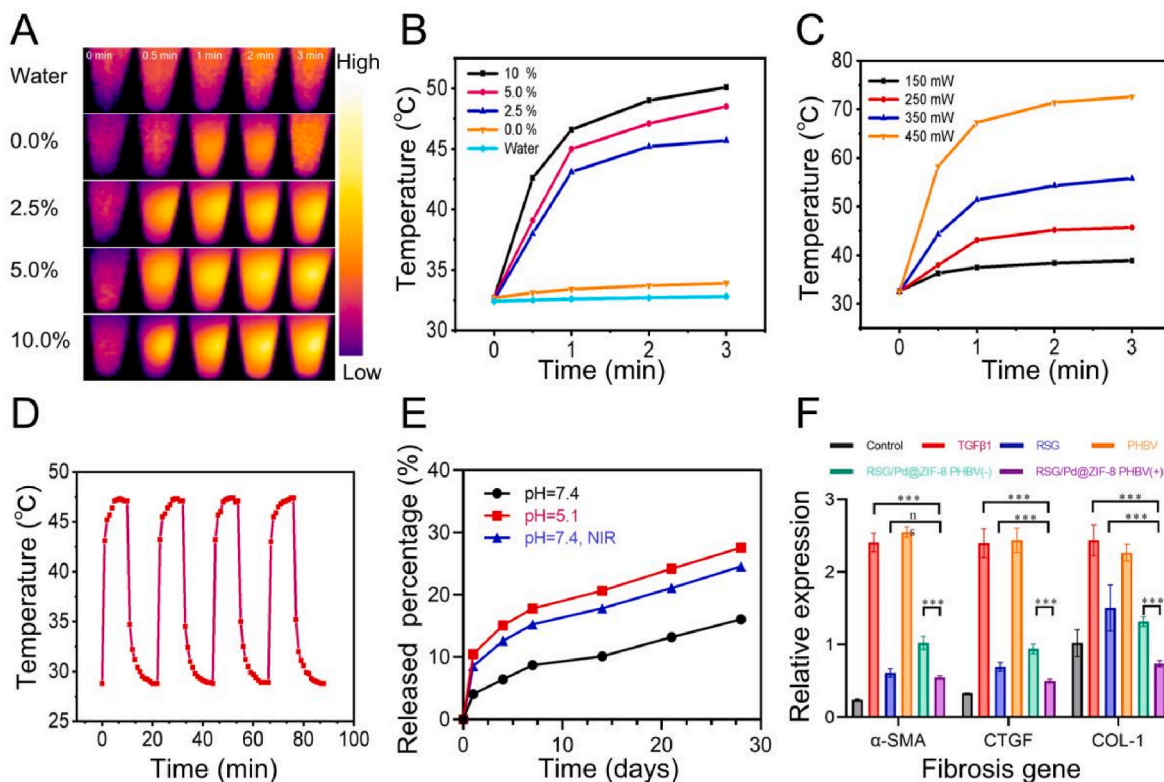


**Fig. 4.** Thermo images (A) and temperature rising profile of different concentration of RSG/Pd@ZIF-8 PHBV films (B) and different laser powers with 2.5 % NPs/PHBV (C). Temperature variation curve of RSG/Pd@ZIF-8 PHBV films (D). The RSG release curve of RSG/Pd@ZIF-8 PHBV films (E). The RSG/Pd@ZIF-8 PHBV films alters the expression of fibrosis genes in HTFs (F).
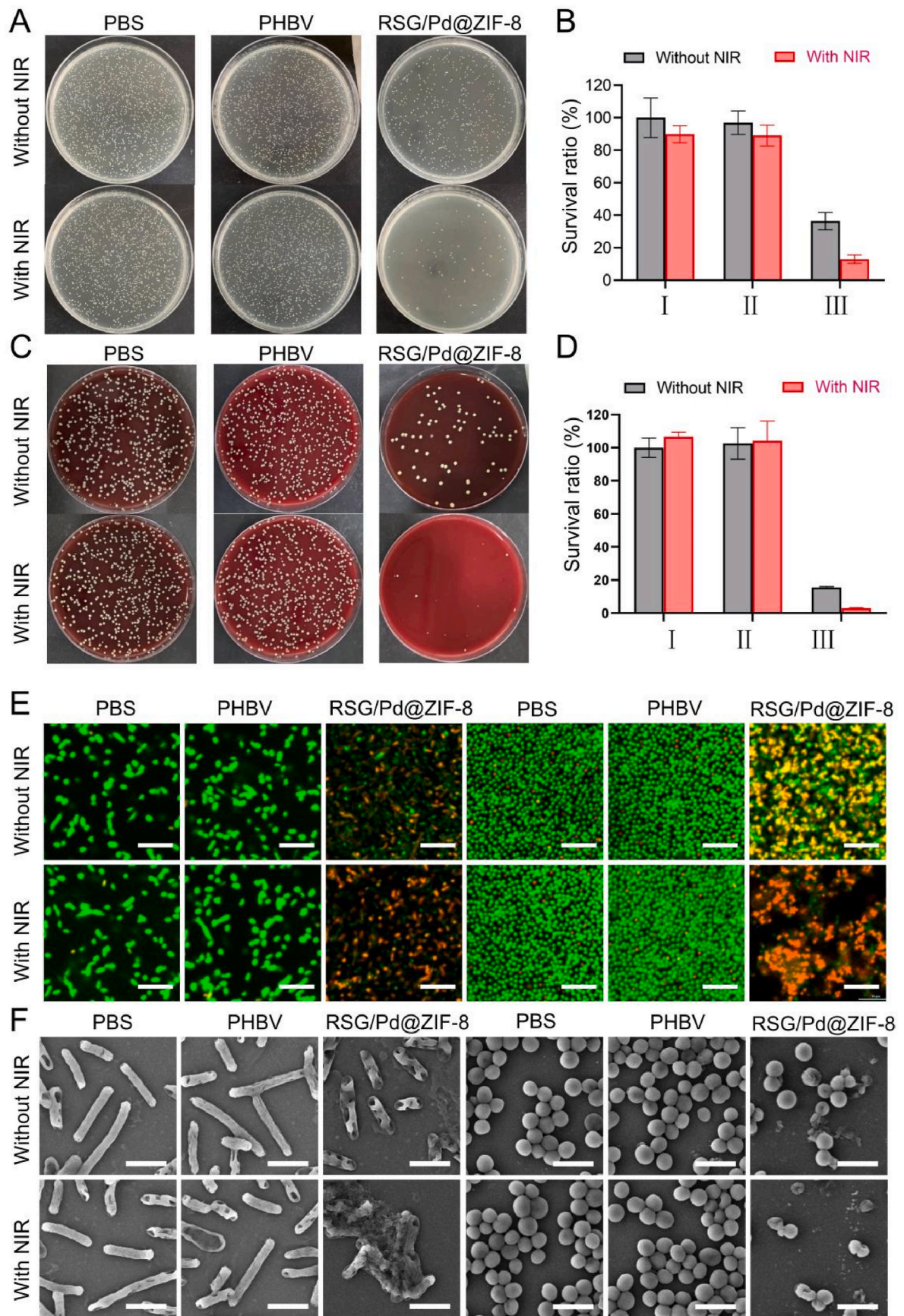
**Fig. 5.** *E. coli* and *S. aureus* in bacteria plate test (A&C) and their colony count statistics (B&D). Fluorescence images (E) of *E. coli* and *S. aureus*. SEM images (F) of *E. coli* and *S. aureus*.
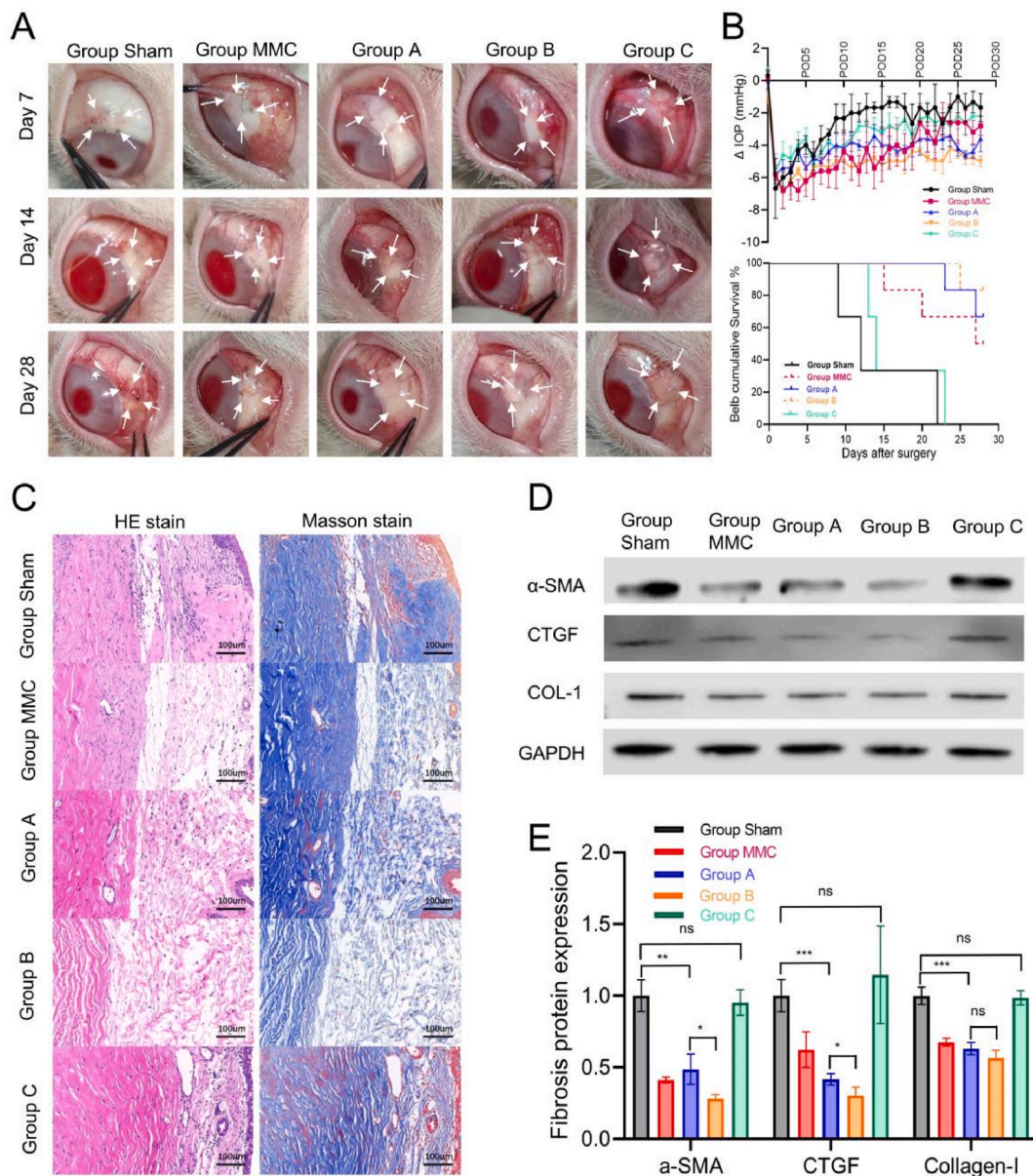
**Fig. 6.** Morphology (A) of filtering blebs after trabeculectomy; white arrows display the range of filtering blebs. Image (B) displays postoperative changes of IOP (top) and survival curve of filtering blebs (bottom). The HE and Masson stain images of blebs (C). Western blot results (D&E) of fibrosis protein from blebs.

appeared in the sham group and group C. In contrast, group MMC, group A and group B had diffused and elevated filtering blebs without blood vessels. Intraocular pressure (IOP) in rabbits was measured using icare-tonovet on both the operative and non-operative eyes. The sham group and group C exhibited the least effective reduction in IOP, while group B showed the greatest reduction in IOP, followed by group A and MMC (Fig. 6B). Furthermore, the survival curve of filtering blebs was plotted based on bleb morphology and IOP (Fig. 6C). We assessed the morphology of filtration blebs (Supplementary Table 1) based on Indiana bleb appearance grading scale (IBAGS, Supplementary Table 2). On the 28th day after surgery, no functional filtering blebs were observed in the sham group and group C. However, the survival rate of filtering blebs in group B, group A, and group MMC was 83.3 %, 66.7 %, and 50 % respectively. Tissue samples from the filtering blebs were subjected to HE and Masson staining (Fig. 6D). The blebs in the sham group and group C exhibited compact subconjunctival tissue with disordered collagen arrangement and extensive neovascularization. In contrast, the blebs in group B, group A, and MMC showed loose subconjunctival tissue

without disordered collagen or neovascularization. The mechanism of anti-scarring was further examined at the protein level using Western blot analysis (Fig. 6E). The results indicated no significant differences in α-SMA (alpha-smooth muscle actin), CTGF (Connective Tissue Growth Factor), and Collagen I levels between the sham group and group C. Compared to the sham group, group A showed a significant reduction in α-SMA (**p < 0.01), CTGF (***p < 0.001), and Collagen I (***p < 0.001). Group B, which received a sustained film with 808 nm laser irradiation, exhibited significantly lower levels of α-SMA (*p < 0.05) and CTGF (*p < 0.05) compared to group A, as well as a lower level of Collagen I, although the difference was not statistically significant.

### 2.9. In vivo biosafety study

Pathological sections of the heart, liver, spleen, lungs, and kidneys revealed no pathological changes in any of the experimental groups (Fig. 7A). H&E staining images of cornea and retina also revealed no pathological changes(Fig. S9). Blood samples were collected from the
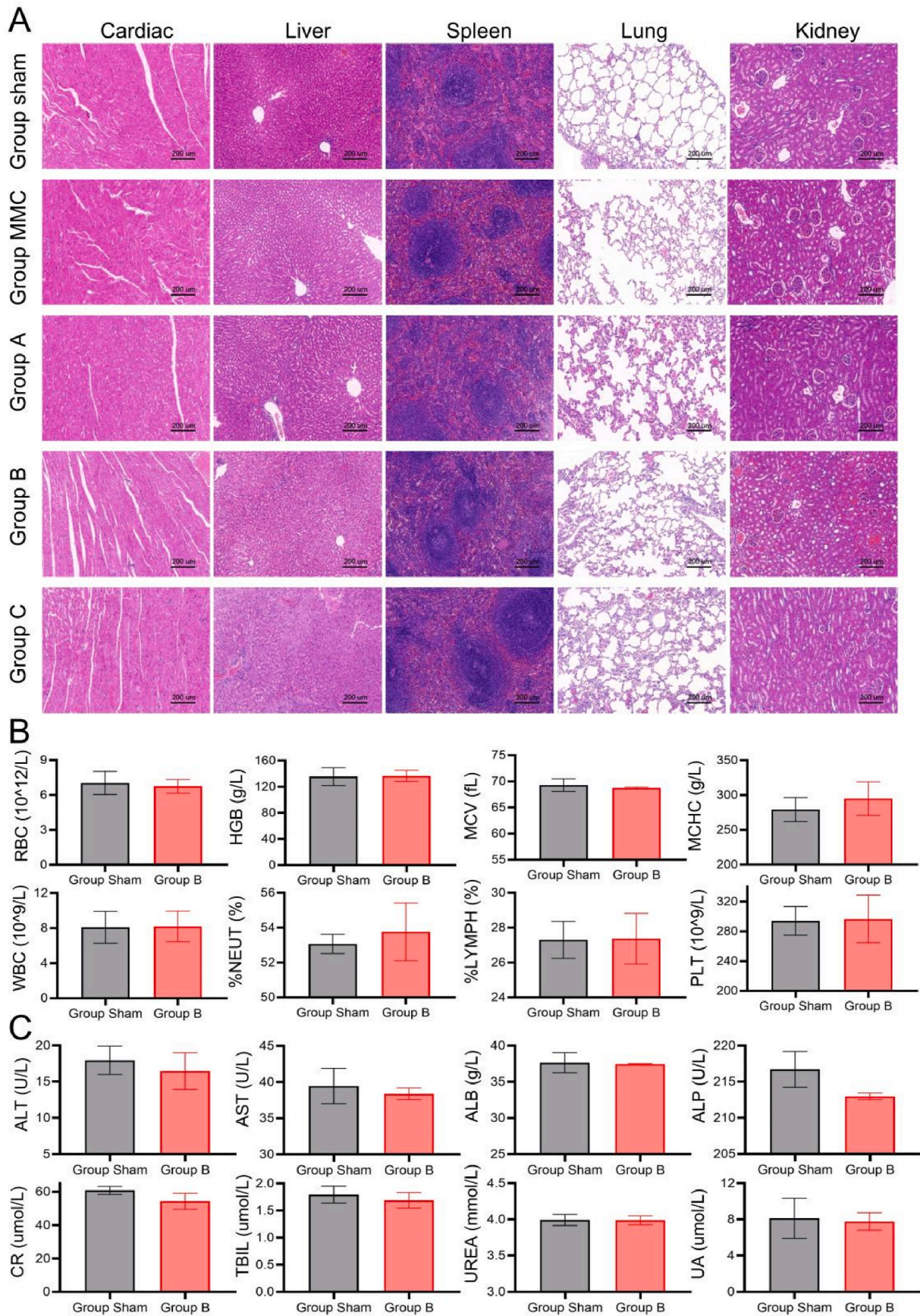
**Fig. 7.** (A) Pathological images of viscera in New Zealand rabbits. (B) Blood routine of New Zealand rabbits. (C) Blood biochemical examination (hepatic & renal function) of New Zealand rabbits.

experimental rabbits to conduct blood routine tests (Fig. 7B) and liver and kidney function tests (Fig. 7C). No significant differences were observed between the sham group and group B in any of the data.

## 3. Conclusion

The RSG/Pd@ZIF-8 NPs drug loading system was successfully synthesized using the Water-DMSO system, demonstrating high drug loading capacity and low cytotoxicity. The RSG/Pd@ZIF-8 PHBV film was successfully prepared via the electrospinning method. The film possesses dual-responsive drug release to near-infrared (NIR) and pH, along with *in vitro* photothermal imaging capabilities. The RSG/Pd@ZIF-8 PHBV film exhibits antibacterial and anti-fibrotic effects, which are further enhanced with NIR irradiation *in vitro*. Implantation of the RSG/Pd@ZIF-8 PHBV film in the eyes of rabbits undergoing trabeculectomy does not cause systemic adverse reactions. The film effectively reduces scar formation, improves the survival rate of filtering blebs, and decreases postoperative IOP. When NIR laser irradiation is applied, the long-term success rate of the surgery is higher, with fewer local side effects compared to MMC.

## 4. Experimental section

**4.1 Materials.** Palladium acetylacetonate, Polyvinylpyrrolidone (PVP), Sodium bromide (NaBr), Dimethyl sulfoxide (DMSO) and N, N-dimethylacetamide (DMA) were purchased from Sinopharm Group Chemical reagent Co., Ltd. (Shanghai, China). Zinc nitrate hexahydrate $(Zn(NO_3)_2 \cdot 6H_2O)$ and 2-methylimidazole (2-mim) were purchased from Sigma-Aldrich (USA). Rosiglitazone was manufactured by Solarbio (Beijing, China). Polyhydroxybutyrate valerate (PHBV) was provided by Hunan University (Changsha, China). Trichloromethane (TCM) and dimethylformamide (DMF) were purchased from Aladdin (Shanghai, China). Cell Counting Kit-8 (CCK-8) were purchased from Biosharp (Hefei, Anhui, China). TGF-β1 were purchased from Proteintech Group, Inc (USA). PCR primers were designed and synthesized by Sangon Biotech (Shanghai, China). Bacteriological petri dishes were purchased from Jiangsu province. LIVE/DEADBacLight were produced by Invitrogen (USA). α-SMA, CTGF and Collagen-I antibodies were purchased from Santa Cruz Biotechnology, Inc. (USA). Hematoxylin-Eosin (HE) Staining Kit and Masson Staining Kit were purchased from Wuhan Servicebio Technology Co., Ltd (Wuhan, Hubei, China). Other conventional consumables for cell culture were purchased from Sigma-Aldrich (USA).

### 4.1. Instrument and characteristics

The morphology and ultra microstructure of ZIF-8, Pd@ZIF-8, RSG/Pd@ZIF-8 NPs and RSG/Pd@ZIF-8 PHBV were examined by scanning electron microscopy (SEM, JEOL, JSM-6700F) and transmission electron microscope (TEM, JEOL, JEM-2100F). Dynamic light scattering (DLS) and zeta potential were measured by Malvern Zetasizer Nano ZS90 (Malvern). We used UV–vis spectrometer (UV-2450, Shimadzu) to acquire the absorbance of samples. TENSOR27 spectrometer (Bruker) was used to record fourier transform infrared (FTIR) spectra of tested samples. The X-Ray Diffraction (XRD) patterns were collected on a PANalytical X'Pert Pro diffractometer. The NIR (808 nm) laser (Beijing Keplin Optoelectronic Technology Co., Ltd., China) and infrared thermal imaging camera (E60, FLIR, USA) were used to investigate *in vitro* photothermal experiments. The absorbance of samples was measured at a wavelength of 570 nm and 630 nm using an infinite M200 microplate reader (Tecan, Switzerland).

### 4.2. Synthesis of RSG/Pd@ZIF-8 NPs

In a high-pressure reaction bottle, add 20 mg of palladium, 60 mg of PVP, and 20 mg of NaBr in sequence to 4 mL of N, N-dimethylacetamide

(DMA) and 8 mL of water. Dissolve them completely under magnetic stirring. Under carbon monoxide (CO) protection at a pressure of 1 atm, heat the mixed solution in a methyl silicone oil bath while stirring magnetically. Slowly raise the temperature to 100 °C within 30 min and maintain it at 100 °C for 90 min to obtain a Pd nanosheets/PVP solution with a concentration of 0.6 mg/mL. Transfer 2 mL of the Pd nanosheets/PVP solution into a 50 mL centrifuge tube and mix it with 28 mL of acetone solution. Centrifuge the mixture at 5000 rpm for 10 min, discard the supernatant, and collect the Pd nanosheets for later use.

To prepare the ZIF-8 and Pd@ZIF-8 NPs, dissolve 0.23 g of Zn(NO3)2·6H2O in 2.5 mL of distilled water (solution A), and dissolve 0.515 g of 2-Methylimidazole in 2 mL of distilled water (solution B). Dissolve 2 mg of Pd nanoparticles and 60 mg of rosiglitazone in 5 mL of DMSO to obtain solution C. In a glass bottle placed in a 25 °C water bath, mix 5 mL of solution C and 2.5 mL of solution A, and stir magnetically for 5 min. Then, add solution B dropwise while continuing magnetic stirring for 1 h to obtain a white solution. Centrifuge the white solution at 8000 rpm for 5 min, discard the supernatant, and collect the white precipitate. Wash the precipitate three times with 50 % ethanol and dry it in a 60 °C oven to obtain RSG/Pd@ZIF-8 NPs. By replacing solution C with pure DMSO solution or DMSO solution containing 2 mg of Pd nanosheets, the remaining steps remain unchanged, and ZIF-8 and Pd@ZIF-8 NPs can be obtained. Similar preparation methods have been reported previously. The calculation of drug loading and encapsulation efficiency was based on previous reports [28].

### 4.3. Synthesis of RSG/Pd@ZIF-8 PHBV film

Weigh the PHBV powder and dissolve it in TCM solution. Stir the mixture magnetically at 60 °C for 20–30 min until it becomes colorless and transparent, resulting in a PHBV-TCM solution with a concentration of 55.6 mg/mL. Prepare this solution for later use. Dissolve the RSG/Pd@ZIF-8 nanoparticles in DMF. Then, add the DMF solution containing the nanoparticles to the PHBV-TCM solution at 60 °C for 10 min to obtain a bluish-black spinning solution for electrospinning. The TCM: DMF ratio is 9:1, and the concentration gradient is set with different weight ratios of nanoparticles to PHBV (0 %, 2.5 %, 5.0 %, and 10 %).

The electrospinning parameters are as follows: the voltage is set at 15 kV, the distance between the syringe needle and the receiving plate is 15 cm, and the injection pump operates at an advancing speed of 5 mL/h. For each film, 3 mL of the final spinning solution with a PHBV concentration of 50 mg/mL is used. After spinning, the membranes are placed under a fume hood for 3 days to allow for complete removal of the volatile organic solvent.

### 4.4. Cytotoxicity study

The steps for the CCK-8 test of RSG/Pd@ZIF-8 NPs are as follows: In a 96-well plate, $5 \times 10^3$ human Tenon's capsule fibroblast cells (HTFs, Otwo Biotech Inc.) were added to each well (100 μL/well). Rosiglitazone/Pd@ZIF-8 and Pd@ZIF-8 NPs were added to each well at the concentrations of 0 μg/mL (control group), 10 μg/mL, 20 μg/mL, 30 μg/mL, 40 μg/mL, 50 μg/mL, and 60 μg/mL. A blank control group without cells was also set up with an equal amount of cell culture medium. Each group had 5 replicate wells and was incubated at 37 °C with 5 % carbon dioxide for 24 h. Afterward, 10 μL of CCK-8 reagent was added to each well, gently shaken, and incubated for 2 h at 37 °C with 5 % carbon dioxide. The absorbance of each well at 570 nm was measured using a UV spectrophotometer, excluding the maximum and minimum values of each group. The average of the remaining three values was calculated.

The steps for the CCK-8 test of RSG/Pd@ZIF-8 PHBV films are as follows: A 1 cm diameter film with different concentrations (0 %, 2.5 %, 5 %, 10 %) was added to each well of a 24-well plate, with 5 replicate wells for each group. 200 μL of DMEM medium containing 10 % Fetal bovine serum was added to each well, fully immersing the films. The

plate was then placed under the condition of 37 °C with 5 % carbon dioxide for 24 h. After removing the culture solution from the wells, 400 μL of HTFs containing $2 \times 10^4$ cells was added to each well. The cells were incubated at 37 °C with 5 % carbon dioxide for 24 h. The absorbance at 570 nm was measured using the same steps as described above for the CCK-8 test of RSG/Pd@ZIF-8 NPs. The average value was calculated, excluding the maximum and minimum values.

### 4.5. Hemolysis test

Take 50 mg of films and place them in individual 1.5 mL centrifuge tubes. Add 0.5 mL of PBS to each tube, ensuring that the films are fully immersed. For the positive control, use pure water, and for the negative control, use PBS. Add 0.5 mL of rabbit blood to each centrifuge tube and mix thoroughly for 3 h. Afterward, centrifuge each group of solutions at high speed (10,000 rpm) for 3 min. Measure the absorbance of the supernatant at a wavelength of 545 nm. Calculate the hemolysis rate using the following formula.

### 4.6. Cell adhesion experiment

After co-culturing the films with HTFs cells for 24 h (as described in the previous section for the CCK-8 test), remove the culture medium and rinse the films twice with PBS. Then, perform a gradient dehydration process by sequentially adding 50 %, 60 %, 70 %, 80 %, 90 %, and 100 % ethanol for 15 min at each concentration. Remove the absolute ethanol and add an electron microscope fixative (Glutaraldehyde) to the films, allowing them to incubate for 2 h at room temperature.

Next, place the films on the sample stage of an ion sputtering instrument and apply a gold coating for 30 s. Using the low vacuum mode, observe the surface morphology of the samples under a voltage of 1 kV.

### 4.7. Photothermal effect

The films were immersed in $ddH_2O$ for photothermal evaluation, with $ddH_2O$ serving as the control. Temperature changes were recorded using FLIR imaging instruments while irradiating the films with an 808 nm NIR laser.

### 4.8. Drug release

Take a 100 mg film and place it in a 10 mL centrifuge tube containing 5 mL of $ddH_2O$. Maintain the experimental environment at a constant temperature of 37 °C and shake the tube at 50 rpm. At days 1, 4, 7, 14, 21, and 28, measure the absorbance of the film extracts at a wavelength of 315 nm using a UV spectrophotometer.

### 4.9. In vitro anti-fibrosis effect of RSG/Pd@ZIF-8 PHBV film

To evaluate the anti-fibrosis effect *in vitro*, $2 \times 10^6$ HTFs were seeded onto 6 cm dishes containing circular films with a diameter of 2 cm. TGF-β1 was added to induce the differentiation of fibroblasts (HTFs) into myofibroblasts [29]. All tested specimens were cultured in a humidified incubator at 37 °C with 5 % $CO_2$. In the 808 nm laser irradiation group, the parameters used were a power of 250 mW and a duration of 5 min. After 24 h of *in vitro* culture, the transcriptional levels of fibrosis-related genes were assessed using RT-qPCR assay. The primer sequences for the tested genes in the RT-qPCR assay are presented in Supplementary Table 3.

### 4.10. Antibacterial activity

To test the *in vitro* antibacterial properties of the RSG/Pd@ZIF-8 PHBV film, *S. aureus* and *E. coli* were used as model bacteria. The six experimental groups were as follows: (1) PBS, (2) PBS + NIR, (3) PHBV film, (4) PHBV film + NIR, (5) RSG/Pd@ZIF-8 PHBV film, and (6) RSG/

Pd@ZIF-8 PHBV film + NIR. The NIR groups were subjected to treatment with an 808 nm laser at a power density of 250 mW/cm$^2$ for 5 min.

In each experiment, 5 mL of bacterial solution was added to a 10 mL centrifuge tube containing 5 mg of the respective films. The tubes were then incubated at 37 °C for 2 h. Subsequently, 100 μL of each solution from the different groups was spread onto blood agar and solid agar plates. The plates were cultured for 20 h at 37 °C, and the colony-forming units (CFUs) were counted for each group.

To assess bacterial morphology and viability, live/dead assays were performed using the LIVE/DEAD BacLight Bacterial Viability Kits (Invitrogen), following the procedures described in a previous study [30].

### 4.11. Experimental study on in vivo anti scar effect

In the *in vivo* study on rabbits, trabeculectomy was performed using the following procedure. After achieving adequate anesthesia, the surgical area in the upper temporal region of New Zealand White Rabbit eyes was selected, avoiding interference from the third eyelid. A conjunctival flap measuring 5 mm × 5 mm, based on the fornix, was created. Under the conjunctival flap, a scleral flap measuring 3 mm × 3 mm and 1/2 scleral thickness was made. At the root of the scleral flap (corneoscleral limbus), a 2 mm long and 0.5 mm wide incision was made. Through this incision, a tissue piece measuring approximately 2 mm × 2 mm, including the inner sclera, trabecular tissue, and iris, was removed.

The tested rabbits were divided into five groups: (1) group Sham, (2) group MMC, (3) group A, (4) group B, and (5) group C. Group Sham served as the negative control, undergoing a simple trabeculectomy without any implantation. Group MMC, the positive control, underwent the commonly used clinical method of placing a sponge containing 0.4 mg/mL of MMC under the scleral and conjunctival flaps for 3 min during surgery. Group A and B were implanted with RSG/Pd@ZIF-8 PHBV film on the scleral flap, and group B received additional treatment with an 808 nm laser. Group C was implanted with PHBV film alone.

Intraocular pressure (IOP) measurements were taken at 10 a.m. the day before anesthesia, serving as the baseline IOP. Rabbits with abnormal baseline IOP were excluded from the study. From the second day to the 28th day after surgery, IOP was measured using iCare-Tonovet in the experimental and control eyes of the rabbits every day at 10 a.m. The Indiana Bleb Grading Appearance Scale (IBGS) system was used to evaluate the survival of filtering blebs, and weekly photographs were taken to document the morphology of the filtering blebs.

On the 28th day after surgery, the rabbits were euthanized, and tissue samples from the filtering blebs were collected. H&E staining and Masson staining were performed following established protocols from previous research. Additionally, Western blot experiments were conducted using a portion of the tissue, similar to previous studies.

Rabbit blood is obtained through the rabbit ear vein (Rabbit auricular vein) and centrifuged or precipitated according to different testing requirements. We selected ALT (Alanine aminotransferase), AST (Aspartate aminotransferase), ALB (albumin), ALP (Alkaline phosphatase), TBIL (Total bilirubin) as the indicator for evaluating liver function, while CR (Creatinine), Urea, and UA (Uric acid) were indicators for renal function.

### 4.12. Biosafety evaluation

Local adverse reactions after trabeculectomy were carefully observed and recorded, including conjunctival edema, conjunctival congestion, corneal toxicity, filtration bubble leakage, and endophthalmitis.

On the 28th day post-surgery, the experimental rabbits were euthanized, and small samples of heart, liver, spleen, lung, and kidney tissue were collected. These tissues were immersed in 10 % formalin and fixed for 2 days. Paraffin sections were then prepared, followed by H&E

staining. A pathologist evaluated the stained sections under a microscope to assess any histopathological changes.

Peripheral venous blood samples were collected from the rabbits for blood routine and biochemical tests, specifically assessing liver and kidney function. These tests aimed to evaluate the potential impact of the implants on the systemic system of the rabbits.

### 4.13. NIR laser irradiation parameters

This study selected laser parameters with a power of 250 mW, a distance of 2 cm and an irradiation time of 5 min for *in vivo* and *in vitro* experiments including antibacterial, drug release, cell and animal tests.

### 4.14. Statistical analysis

All data are expressed as mean $\pm$ standard deviation at least n = 3. Statistical analysis was performed using the GraphPad Prism 8 software. The differences were considered at $p < 0.05$ (*), $p < 0.01$ (**), and $p < 0.001$ (***).

### CRediT authorship contribution statement

**Dengming Zhou:** Conceptualization, Data curation, Formal analysis, Investigation, Methodology, Project administration, Resources, Validation, Visualization, Writing - original draft, Writing - review & editing. **Wenxiang Zhu:** Conceptualization, Data curation, Formal analysis, Investigation, Methodology, Software, Validation, Visualization, Writing - original draft, Writing - review & editing. **Hairong Liu:** Conceptualization, Data curation, Formal analysis, Project administration, Software, Visualization, Writing - review & editing. **Feng Zhang:** Conceptualization, Data curation, Project administration, Resources, Software, Supervision, Validation. **Xiaoyu Zhou:** Data curation, Investigation, Methodology, Software, Supervision, Visualization. **Xinyue Zhang:** Formal analysis, Investigation, Methodology, Resources, Software, Supervision. **Yang Zhao:** Data curation, Formal analysis, Methodology, Project administration, Resources, Software. **Yuting Huang:** Data curation, Formal analysis, Project administration, Resources, Validation, Visualization. **Xuanchu Duan:** Conceptualization, Data curation, Funding acquisition, Investigation, Methodology, Software, Supervision, Validation, Visualization, Writing - review & editing.

### Declaration of competing interest

The authors declare that they have no known competing financial interests or personal relationships that could have appeared to influence the work reported in this paper.

### Data availability

No data was used for the research described in the article.

### Acknowledgements

### Appendix A. Supplementary data

Supplementary data to this article can be found online at https://doi.org/10.1016/j.mtbio.2023.100922.

### References

[1] Y.C. Tham, X. Li, T.Y. Wong, H.A. Quigley, T. Aung, C.Y. Cheng, Ophthalmology 121 (11) (2014) 2081–2090.
[2] J.B. Jonas, T. Aung, R.R. Bourne, A.M. Bron, R. Ritch, S. Panda-Jonas, Lancet 390 (10108) (2017) 2183–2193.
[3] R.N. Weinreb, T. Aung, F.A. Medeiros, J. Am. Med. Assoc. 311 (18) (2014) 1901–1911.
[4] H.A. Alkozi, G. Navarro, R. Franco, J. Pintor, Prog. Retin. Eye Res. 75 (2020), 100798.
[5] P.J. Ernest, J.S. Schouten, H.J. Beckers, F. Hendrikse, M.H. Prins, C.A. Webers, Ophthalmology 120 (3) (2013) 512–519.
[6] F.A. Medeiros, L.M. Alencar, P.A. Sample, L.M. Zangwill, R. Susanna, R. N. Weinreb, Ophthalmology 117 (11) (2010) 2061–2066.
[7] European glaucoma society terminology and guidelines for glaucoma, Br. J. Ophthalmol. 105 (Suppl 1) (2021) 1–169, 5th Edition.
[8] J.D. Stein, A.P. Khawaja, J.S. Weizer, J. Am. Med. Assoc. 325 (2) (2021) 164–174.
[9] G. Sunaric Megevand, A.M. Bron, Prog. Retin. Eye Res. 81 (2021), 100879.
[10] H. Mazdak, I. Meshki, F. Ghassami, Eur. Urol. 51 (4) (2007) 1089–1092.
[11] D.Y. Yu, W.H. Morgan, X. Sun, E.N. Su, S.J. Cringle, P.K. Yu, P. House, W. Guo, X. Yu, Prog. Retin. Eye Res. 28 (5) (2009) 303–328.
[12] J. Berger, D.E. Moller, Annu. Rev. Med. 53 (2002) 409–435.
[13] G. Musso, M. Cassader, E. Paschetta, R. Gambino, JAMA Intern. Med. 177 (5) (2017) 633–640.
[14] M.S. Joy, D.S. Gipson, M. Dike, L. Powell, A. Thompson, S. Vento, A. Eddy, A. B. Fogo, J.B. Kopp, D. Cattran, H. Trachtman, Clin. J. Am. Soc. Nephrol. 4 (1) (2009) 39–47.
[15] D.T. Chan, G.F. Watts, A.B. Irish, G.K. Dogra, Nephrol. Dial. Transplant. 26 (11) (2011) 3543–3549.
[16] E.M. Toledo, N.C. Inestrosa, Mol. Psychiatr. 15 (3) (2010) 272–285.
[17] T. Genovese, S. Cuzzocrea, R. Di Paola, E. Mazzon, C. Mastruzzo, P. Catalano, M. Sortino, N. Crimi, A.P. Caputi, C. Thiemermann, C. Vancheri, Eur. Respir. J. 25 (2) (2005) 225–234.
[18] F. Zhang, K. Liu, M. Cao, J. Qu, D. Zhou, Z. Pan, X. Duan, Y. Zhou, Invest. Ophthalmol. Vis. Sci. 60 (7) (2019) 2743–2752.
[19] F. Zhang, K. Liu, Z. Pan, M. Cao, D. Zhou, H. Liu, Y. Huang, X. Duan, Drug Deliv. 26 (1) (2019) 812–819.
[20] J. Liang, G. Huang, X. Liu, F. Taghavifar, N. Liu, Y. Wang, N. Deng, C. Yao, T. Xie, V. Kulur, K. Dai, A. Burman, S.C. Rowan, S.S. Weigt, J. Belperio, B. Stripp, W. C. Parks, D. Jiang, P.W. Noble, J. Clin. Invest. 132 (11) (2022), e157338.
[21] J. Wang, Y. Song, L. Elsherif, Z. Song, G. Zhou, S.D. Prabhu, J.T. Saari, L. Cai, Circulation 113 (4) (2006) 544–554.
[22] A. Giménez, A. Parés, S. Alié, J. Camps, R. Deulofeu, J. Caballería, J. Rodés, J. Hepatol. 21 (3) (1994) 292–298.
[23] M.F. Escobedo Monge, E. Barrado, C. Alonso Vicente, M.P. Redondo Del Río, J. M. Marugán de Miguelsanz, Nutrients 11 (1) (2019) 150.
[24] W. Zhu, M. Chen, Y. Liu, Y. Tian, Z. Song, G. Song, X. Zhang, Nanoscale 11 (43) (2019) 20630–20637.
[25] Z. Qian, N. Zhao, C. Wang, W. Yuan, J. Mater. Sci. Technol. 127 (2022) 245–255.
[26] H.S. Kim, J. Chen, L.P. Wu, J. Wu, H. Xiang, K.W. Leong, J. Han, J. Tissue Eng. 11 (2020), 2041731420949332.
[27] Y. Li, R. Zhong, Z. Zhou, H. Liu, Y. Dai, Y. Hu, J. Appl. Polym. Sci. 137 (2020), 48378.
[28] H. Zheng, Y. Zhang, L. Liu, W. Wan, P. Guo, A.M. Nyström, X. Zou, J. Am. Chem. Soc. 138 (3) (2016) 962–968.
[29] Y. Zhao, F. Zhang, Z. Pan, H. Luo, K. Liu, X. Duan, Cell Death Dis. 10 (8) (2019) 594.
[30] W. Zhu, Z. Zhou, Y. Huang, H. Liu, N. He, X. Zhu, X. Han, D. Zhou, X. Duan, X. Chen, Y. He, X. Meng, S. Zhu, J. Mater. Sci. Technol. 136 (2023) 200–211.